Electron-beam instabilities in the foreshock of high-Mach-number oblique shocks

Martin S. Weidl,[a,*] **Artem Bohdan,**[b] **Paul J. Morris**[b] **and Martin Pohl**[b,c]

[a]*Max-Planck-Institut für Plasmaphysik, Boltzmannstr. 2, DE-85748 Garching, Germany*
[b]*DESY, DE-15738 Zeuthen, Germany*
[c]*Institute of Physics and Astronomy, University of Potsdam, DE-14476 Potsdam, Germany*
   E-mail: martin.weidl@ipp.mpg.de

Motivated by simulations of non-relativistic high-Mach-number shocks in supernova remnants, we investigate the instabilities excited by relativistic electron beams in the extended foreshock of oblique shocks. The phase-space distributions in the near and far upstream of the PIC simulation of a shock are used as initial conditions for simulations with periodic boundary conditions to study their relaxation towards equilibrium. We find that the observed electron-beam instabilities agree very well with the predictions of a linear dispersion analysis: the electrostatic electron-acoustic instability dominates in the far upstream of the foreshock, while the denser electron beams in the near upstream drive the gyroresonant oblique-whistler instability.

---

*Presenter

1. Introduction

Galactic cosmic-ray particles are assumed to receive their TeV-scale energies predominantly from acceleration in non-relativistic collisionless shocks in the environment of supernova remnants (SNRs). Although ions can generally reach higher energies in shock-acceleration processes, understanding the role of electrons is also crucial to interpret observations of X-ray synchrotron radiation at SNR shocks correctly. Here we study the role of beam instabilities in the electron foreshock of oblique shocks.

The mechanisms through which electrons are accelerated at perpendicular shocks with a high Alfvénic Mach number ($M_A \sim 30$) are well known [1]. More recently, the importance of shock-accelerated electrons which may be reflected back into the upstream plasma at quasi-perpendicular shocks has been highlighted [2]. If these reflected electrons stream along the oblique magnetic field and excite sufficiently strong electromagnetic instabilities in the electron foreshock, they may undergo a Fermi-like acceleration process and reach superthermal energies.

In the context of bow shocks with lower Mach numbers ($M_A \lesssim 20$), the instabilities which may arise in electron foreshocks have long been studied in the space-physics community [3–5]. More recently, particle-in-cell (PIC) simulations of the electrostatic two-beam instability, the electromagnetic oblique-whistler instability and the anisotropy-driven whistler heat-flux instability (WHFI) have become possible [6, 7]. These previous simulations used initial conditions that correspond to solar-wind observations, often with a larger beam anisotropy than one would expect for a shock-reflected beam. For the results presented here, our initial phase space is modelled after the electron distribution in the PIC simulation of a high-Mach-number oblique shock.

How we have obtained these distributions is reported in Section 2, followed by a detailed analysis of the electron instabilities that are excited as these distributions relax towards thermal equilibrium. We compare analytic and numerical results for the non-relativistic linear regime with periodic-box simulations that include all relativistic effects. In Section 4, we estimate what these results imply for electron acceleration in high-Mach-number shocks.

2. Shock simulation

First, we analyse a numerical simulation of an oblique collisionless shock to obtain realistic phase-space distributions, from which we can later derive growth rates for electron-beam driven instabilities. We use the fully kinetic PIC code TRISTAN in a 2D3V configuration, evolving the electric and magnetic fields on a two-dimensional Yee grid and the three momentum components of each quasiparticle with a relativistic Vay pusher [8].

The upstream plasma, composed of electrons and protons with density n_0, is initialised uniformly with a drift velocity of $\mathbf{v}_{up}/c = -0.20\hat{x}$ and an isotropic thermal velocity spread with $T_e = T_i = 10^{-3} \ m_e c^2$ and streams left towards the $x = 0$ boundary, which acts as a reflecting conducting wall (i.e. $E_y|_{x=0} \equiv 0$). A uniform magnetic field $\mathbf{B}_0 = B_0(\cos\theta_{Bn}, 0, \sin\theta_{Bn})$ is applied across the simulation domain with an out-of-plane component ($\theta_{Bn} = 60°$, see Figure 1a). Additionally, a drift current is added to the velocity of ions close to the reflecting wall to create a current sheet and smooth artificial peaks in the field gradients [9].
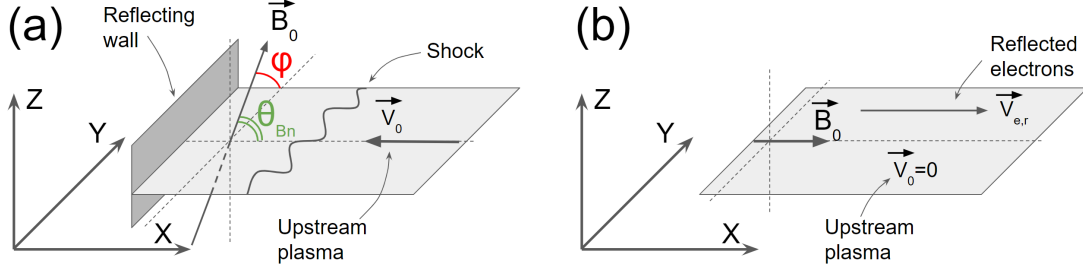
Figure 1: Sketches of the geometries of (a) the shock simulation discussed in Section 2 and (b) the periodic-box simulations of Section 3
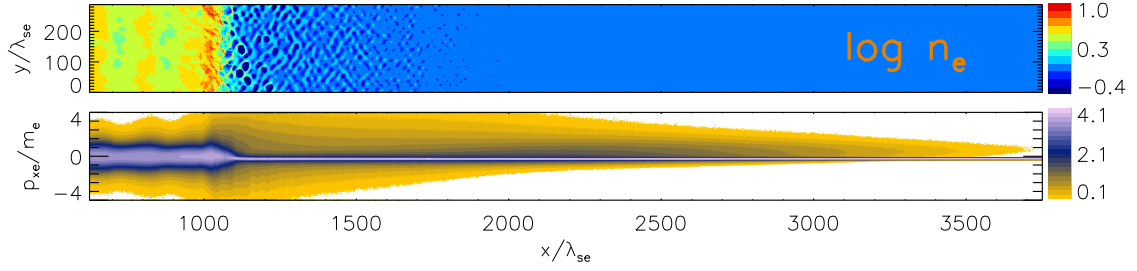

Figure 2: Profile of the electron density (top) and histogram of the x-p_x phase-space density for electrons (bottom) at time $t = 18.1\,\Omega_i^{-1}$

Our simulation assumes an overdense plasma typical of the interstellar medium ($\Omega_e = -eB_0/m = -0.06\,\omega_p$, where ω_p denotes the electron plasma frequency and $\Omega_{e/i}$ represent the signed gyrofrequencies of either species). With a mass ratio $m_p/m_e = 50$, the Alfvén velocity is $v_A = B_0/(n_0 m_0)^{1/2} = 0.0088c$ (using Heaviside–Lorentz units) and an upstream ion gyroradius measures $\rho_i = \gamma_0 v_{\mathrm{up}}/\Omega_i = 5\lambda_{\mathrm{se}}$. The simulation domain is resolved with eight grid points per electron inertial length $\lambda_{\mathrm{se}} = c/\omega_p$ and measures $288\,\lambda_{\mathrm{se}}$ along the y direction and initially $625\,\lambda_{\mathrm{se}}$ in the x direction. During the simulation, the domain length along x increases, as the right wall, at which new upstream plasma is continually injected, is moving outwards at the speed of light. Thus all electrons that get reflected back upstream at the shock front remain in the simulation box.

After enough upstream plasma has been reflected at the left edge, the magnetic field and the plasma in the region downstream of the rightwards-moving density gradient have completely isotropised and reach a compression ratio of close to $n_{\mathrm{dn}}/n_0 = 4.0$. A quasi-stationary shock propagates along the positive x axis with velocity $\mathbf{v}_s^*/c = 0.06\,\hat{x}$ as measured in the simulation frame, corresponding to a shock velocity $\mathbf{v}_s/c = 0.26$ as measured in the upstream frame and an Alfvénic Mach number $M_A = v_s/v_A = 30$.

The electron-density profile after the shock has fully formed, shown in Figure 2, suggests a tripartition of the simulation domain into a downstream region ($x \lesssim 1000\lambda_{\mathrm{se}}$), a near-upstream region ($1000 \lesssim x/\lambda_{\mathrm{se}} \lesssim 2000$), and a far-upstream region ($2000\lambda_{\mathrm{se}} \lesssim x$). While the downstream plasma exhibits turbulence on all length scales below $\lambda \sim 400\lambda_{\mathrm{se}}$, the near upstream is dominated by oblique waves with a wavelength around $\lambda \sim 60\lambda_{\mathrm{se}}$ and a significant magnetic component. In the far-upstream region, the magnetic field stays quiescent in comparison to the strong fluctuations
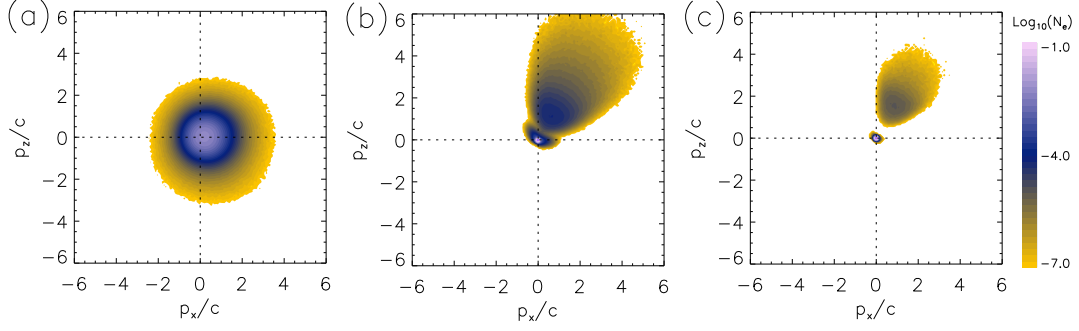
3

Figure 3: Electron momentum distributions projected on the $\mathbf{v}_{\text{sh}}$-$\mathbf{B}_0$ plane in representative sections of the (a) downstream ($125 < x/\lambda_{\text{se}}/250$ in Figure 2), (b) near-upstream ($2500 < x/\lambda_{\text{se}} < 2625$), and (c) far-upstream ($3250 < x/\lambda_{\text{se}} < 3373$) region.

in the electric field, which propagate along the x axis with a wavelength around $\lambda \sim 5\lambda_{\text{se}}$.

Figure 3 shows the $p_x - p_z$ momentum distribution of electrons in three representative regions: for the downstream (electrons with $125 < x/\lambda_{\text{se}}/250$), the near upstream ($2500 < x/\lambda_{\text{se}} < 2625$), and the far upstream ($3250 < x/\lambda_{\text{se}} < 3373$). The selected upstream regions lie where the excitation of oblique electromagnetic and longitudinal electrostatic waves begins to be measurable, but the waves are not strong enough yet to be visible in the density profile in Figure 2. Whereas the electrons are isotropic in the downstream, the upstream contains shock-reflected electrons that are clearly distinct from the background electrons. Although the mean drift between both electron populations is comparable ($v_{\text{dr}} \approx 0.9c$) in both the near and the far upstream, the density of the reflected-electron beam significantly decreases farther upstream. Their momentum spread also becomes smaller with greater distance from the shock, implying that electrons are scattered far more effectively by the electromagnetic waves in the near upstream than by the electrostatic fluctuations in the far upstream.

3. Periodic-boundary-condition simulations

Having identified two modes which are characteristic of the far upstream and the near upstream in our shock simulation, respectively, we explore whether they can be locally excited by beam instabilities or are more likely to have propagated there from the shock. Hence we run two simulations with periodic boundary conditions and start them with initial velocity distributions matching the ones we found in either region. To cover the widest range of propagation angles with respect to $\mathbf{B}_0$, we change to an in-plane magnetic field $\mathbf{B}_0 = B_0\hat{x}$ (Figure 1b). The simulations use periodic boundary conditions and extend over $376\,\lambda_{\text{se}} \times 361\,\lambda_{\text{se}}$ and will thus easily contain the wavelengths observed above.

3.1 Far-upstream conditions

For the far-upstream region, we model the reflected electron beam observed in Figure 3c as being homogeneously distributed throughout the simulation domain, with a beam density $n_b = 2.7 \cdot 10^{-3}\, n_0$, drift velocity $\mathbf{v}_b/c = 0.91\,\hat{x}$, and an isotropic Maxwellian thermal spread with $v_{\text{th},b} = 0.40\,c$. The background electrons with number density $n_0 - n_b$ have no mean drift velocity
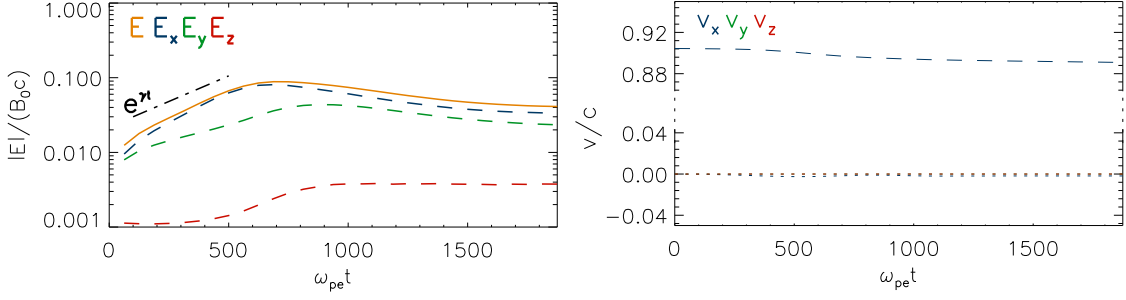
Figure 4: Evolution of (left) electric field and (right) bulk speed of reflected (dashed) and background electrons (dotted), averaged over the entire domain for the far-upstream simulation. The dash-dotted line indicates the peak growth rate $\gamma = 0.07|\Omega_e|$ obtained in a linear dispersion analysis (see text).
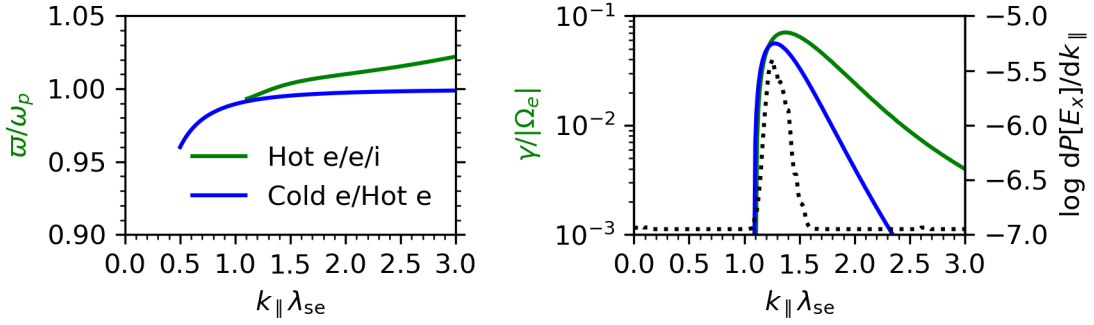

Figure 5: Angular frequency ϖ (left) and growth rate γ (right) of the electron-acoustic instability for far-upstream parameters (blue) and for the numerical solution of the hot-beam dispersion relation (green). For cold-beam and hot-beam calculations, the electrostatic mode reaches a maximum growth rate $\overline{\gamma} = 0.04\,|\Omega_e|$ and $0.07\,|\Omega_e|$, respectively. The dotted line and right-hand axis indicate the power spectrum of E_x at its peak ($\omega_p t = 625$) for the periodic far-upstream simulation.

in the simulation frame, but a thermal spread of $v_{th,0} = 0.07\,c$. The background ions with number density n_0 start with zero mean drift and in temperature equilibrium with the background electrons.

Like in the far-upstream region of the shock simulation, we observe a rapid increase of the electric field component in the drift direction (Figure 4). Although its impact on the bulk speed stays minor, the exponential growth rate we measure ($|E| \propto \exp 0.07|\Omega_e|t$) is so large that the electrostatic waves far upstream of the shock are likely to be created locally by the reflected-electron beam.

This growth rate is also consistent with a linear dispersion analysis of the electron-beam configuration. Figure 5 compares the power spectrum we observe in the periodic simulation with the growth rate for the electron-acoustic instability driven by the relative drift between the two electron populations, the cold background and the hot reflected electrons. The Fourier transform of the electrostatic fluctuations (dotted line, right-hand axis) peaks at $k_\parallel \lambda_{se} \approx 1.3$, in line both with the analytic solution for the electron-acoustic instability (blue line, left-hand axis) and with the numerical solution, which we obtained with WHAMP [10], for the electron-electron-ion system (green line) with the same temperatures as in the simulation. Both solutions of the dispersion relation assume that the velocity distributions of all species follow an isotropic Maxwell distribution.
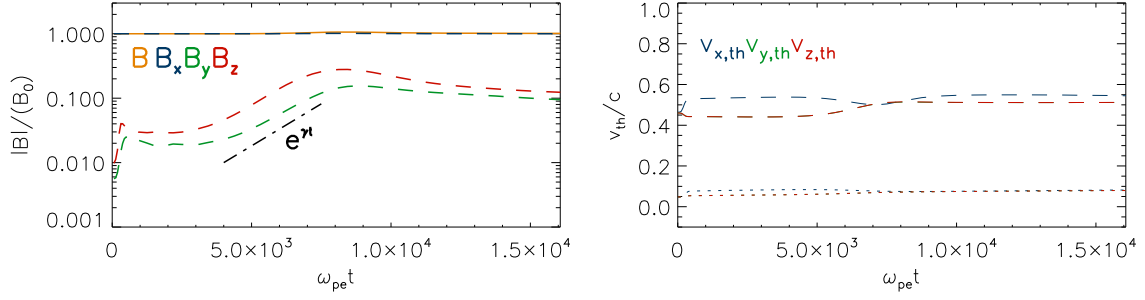
5

Figure 6: Growth of (left) magnetic field and (right) second central moment of the velocities of beam (dashed) and background (dotted) electrons, averaged over the entire domain for the near-upstream simulation (dash-dotted line: linear peak growth rate $\gamma = 0.01|\Omega_e|$)

They do not consider deviations from a Gaussian because of relativistic effects, but they do use the relativistic definition of the beam plasma and cyclotron frequencies, reducing the classical definitions by $\gamma^{1/2}$ and γ, respectively. The agreement between linear theory and simulation is sufficient to unambiguously identify the electron-acoustic instability as the source of the far-upstream electrostatic waves.

The linear dispersion analysis of the far-upstream conditions also predicts an electromagnetic instability at oblique angles, similar to the one described below. However, the growth rate for this oblique mode is so small (below $2 \times 10^{-3} |\Omega_e|$ for all **k**) that its amplitude remains negligible until the shock front arrives. Hence, to explain the oblique waves observed in the shock simulation, we must consider the denser beam of reflected electrons in the near upstream.

3.2 Near-upstream conditions

Thus we set up a second periodic simulation, this time with a phase-space distribution like in Figure 3b. The number density of the reflected-electron beam increases almost tenfold to $n_b = 2.5 \cdot 10^{-2} n_0$. This close to the shock, the thermal spread of the reflected electrons is slightly larger ($v_{\text{th},b} = 0.60\ c$), whereas their mean drift is slightly smaller than before ($\mathbf{v}_b/c = 0.89\ \hat{x}$). On the other hand, the background electrons have already passed through enough waves in the far upstream that their thermal spread has increased to $v_{\text{th},0} = 0.09\ c$. The ion population is initially isothermal with the background electrons.

At first, electrostatic waves develop, similarly to the previous case. But unlike in the far upstream, shortly after the electron-acoustic instability has saturated, the perpendicular magnetic field in near-upstream conditions grows exponentially and saturates within about $5 \times 10^3\ \omega_p^{-1}$ (Figure 6). During this stage of the simulation, the perpendicular thermal velocity of the reflected electrons increases by roughly 12%, after it has remained essentially unaffected by the electrostatic fluctuations before. Simultaneously, the bulk velocity of reflected electrons begins to shrink from the original $v_b/c = 0.89$ to $v_b/c \approx 0.2$, where it eventually stabilises at $\omega_p t \approx 1.5 \times 10^4$ (not shown).

The reason for this burst of perpendicular scattering is the excitation of electromagnetic waves at an angle of about 55° with respect to $\mathbf{B}_0$ (Figure 7). In wavelength and obliquity, these waves agree
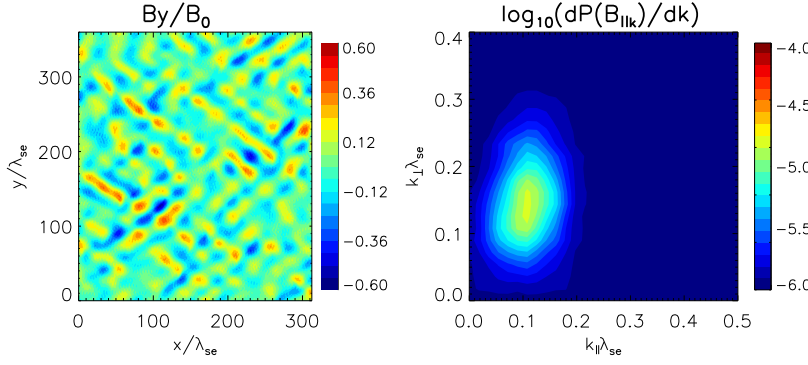
6

Figure 7: 2D profiles of the perpendicular magnetic field B_y at its peak ($\omega_p t = 7500$) in (left) real space and (right) Fourier space for the near-upstream simulation
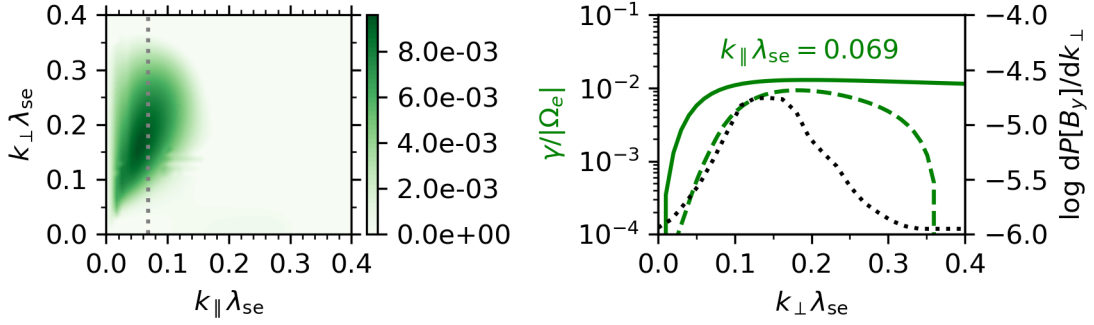

Figure 8: Left: growth rate of oblique electromagnetic mode, calculated with the linear dispersion relation for isotropic hot beams with the near-upstream conditions. Right: growth rate along the gyroresonance condition $k_\parallel \lambda_{se} = 0.069$ for hot beams (dashed line, left-hand axis) and cold beams (solid line) in comparison with the power spectrum of the simulation along its peak ($k_\parallel \lambda_{se} = 0.1$).

extremely well with the fluctuations we pointed out in the near-upstream of the shock simulation (Figure 2).

The strong coupling of these waves to the reflected electrons as well as their distribution in Fourier space, where most of their spectral power lies along the line $k_\parallel \lambda_{se} = 0.1$ (Figure 7), are strong indications that the underlying instability is resonant with the reflected electrons. Indeed, the linear dispersion relation for three hot beams in the near-upstream configuration (Figure 8) predicts unstable waves with similar properties: Their growth rate reaches a maximum value of $\gamma = 0.01|\Omega_e|$ for $(k_\parallel, k_\perp) \approx (0.07\lambda_{se}^{-1}, 0.18\lambda_{se}^{-1})$. Although these waves are not exactly transverse, the magnetic fluctuations have left-handed helicity with respect to $\mathbf{B}_0$, matching the waves we observe both in the periodic and in the shock simulations. For rightwards-travelling waves driven by gyroresonance with the ions, one would expect the opposite helicity (e.g.[11]), and indeed ion terms have only a very small influence on the linear growth rate in this model.

An analytic approximation for the growth rate of an electromagnetic cold-beam instability in this oblique, 'quasi-longitudinal' regime was derived by Stepanov & Kitsenko [12]. In Figure 8, we compare the relativistic version of their result (solid line, left-hand axis) with the growth rate computed for three hot beams (dashed line) at the value of $k_\parallel$ for which the latter rate peaks. The analytic condition for gyroresonance yields a slightly smaller value for $k_\parallel$ ($0.069/\lambda_{se}$) than where

the Fourier transform of the simulation peaks (about $0.10/\lambda_{\mathrm{se}}$), likely because the reflected electrons have been scattered and their bulk speed decreased to $v_b/c = 0.75$ in the simulation. Nevertheless, both curves from linear theory reach a maximum of $\gamma \approx 10^{-2}\,|\Omega_e|$ at a perpendicular wavenumber that is compatible with our periodic simulation.

In the rest frame of the background electrons, the linear calculation for hot beams yields an angular frequency of $\varpi = 0.02\,|\Omega_e|$ for the fastest-growing mode. This is an excellent match for electron gyroresonance ($\varpi - k_\| v_b = 0.9944\,\Omega_e$ or $(\varpi - k_\| v_b - \Omega_e)/(k_\|\sqrt{2}v_{\mathrm{th},b}) = 7{\times}10^{-4}$). Indeed, the analytic approximation we have used is based on a perturbation around this gyroresonance condition. We are currently working on a more detailed description of the coupling mechanism between the two electron species, in order to explain under which conditions the shock-reflected beam is dense enough to drive the oblique whistlers before the shock front arrives.

After the gyroresonant oblique-whistler instability has saturated, both electron species are sufficiently close to equilibrium that no further instability gets excited. The WHFI commonly observed in the solar wind (e.g. [7]) requires a positive beam anisotropy ($T_\perp > T_\|$) for efficient growth, but while the reflected electrons are propagating away from the shock towards a weaker magnetic field, their perpendicular temperature decreases because of adiabatic-moment conservation. Our simulations therefore show no indication that the WHFI is excited. However, the anisotropy of electrons immediately after shock reflection must be studied further as a function of shock parameters.

The magnetic fluctuations in the near upstream of our shock simulation are therefore most likely oblique whistler waves driven by the gyroresonant interaction between the incoming upstream electrons and the shock-reflected electrons.

4. Conclusions

Our 2D shock simulation shows that a beam of relativistic electrons reflected at an oblique shock with $M_A = 30$ can generate an electron-foreshock region with strong electrostatic and electromagnetic waves. This confirms similar observations in a 1D-PIC simulation with $M_A = 63$ [2]. Using linear theory and PIC simulations, we have identified the dominant waves in the far upstream of the foreshock as parallel plasma oscillations driven by the electron-acoustic instability. Closer to the shock front, the foreshock is dominated by oblique whistler waves excited gyroresonantly by the beam of reflected electrons. Similar to ion instabilities at quasi-parallel shocks, these whistler waves scatter the electrons in the foreshock to maintain a steady-state density profile which propagates upstream in front of the shock.

The magnetic-field fluctuations are oblique ($\sim 55°$) with respect to the background field both in the shock simulation, with an out-of-plane component of $\mathbf{B}_0$, and in the periodic near-upstream simulation with an in-plane $\mathbf{B}_0$. The perpendicular beam temperature never grows large enough to excite the parallel WHFI efficiently, contrary to recent simulations of solar-wind conditions [7]. We will publish a more detailed analysis of the evolution of electron scattering and anisotropy in the future.

Acknowledgments

References

[1] Bohdan, A., Niemiec, J., Kobzar, O., et al. 2017, ApJ, 847, 1.

[2] Xu, R., Spitkovsky, A., and Caprioli, D. 2020, ApJL, 897, L41.

[3] Sentman, D. D., Thomsen, M. F., Peter Gary, S., et al. 1983, JGR, 88, 2048

[4] Newman, D. L., Winglee, R. M., and Goldman, M. V. 1988, Phys. Fluids, 31, 1515.

[5] Wong, H. K. and Smith, C. W. 1994, JGR, 99, 13373.

[6] Fu, X. R., Cowee, M. M., Liu, K., et al. 2014, PoP, 21, 042108.

[7] Micera, A., Zhukov, A. N., López, R. A., et al. 2020, ApJL, 903, L23.

[8] Vay, J.-L. 2008, PoP, 15, 056701.

[9] Wieland, V., Pohl, M., Niemiec, J., et al. 2016, ApJ, 820, 62.

[10] Rönnmark, K. 1982, Kiruna Geophys. Inst. – Technical Report.

[11] Weidl, M. S., Winske, D., Jenko, F., et al. 2016, PoP, 23, 122102.

[12] Stepanov, K. N. and Kitsenko, A. B. 1961, Sov. Phys. – Technical Phys., 6, 120.